

## MID-INFRARED IMAGING OF ORION BN/KL. II. LUMINOSITY SOURCES, EXTINCTION DISTRIBUTION, AND THE NATURE OF IRC2

D. Y. GEZARI,<sup>1,2</sup> D. E. BACKMAN,<sup>2,3</sup> AND M. W. WERNER<sup>2,4</sup>

*Received 1997 July 2; accepted 1998 July 17*

### ABSTRACT

We have recalculated the luminosities of IRC2 and the BN Object in the Orion BN/KL complex and determined the distributions of color temperature and silicate absorption-line strength over the region with much greater precision than before, using a complete set of well-sampled and nearly diffraction-limited array camera images of BN/KL at nine wavelengths between 4.8 and 20  $\mu\text{m}$ . We find that the total infrared luminosity of IRC2 itself is only  $L \sim 1000 L_{\odot}$  (much lower than the generally accepted value). However, the temperature and extinction distributions show that the significant luminosity source(s) in BN/KL must still be located within several arcseconds of IRC2. Our results, considered with recent radio continuum and maser emission observations, suggest that a luminous early-type star located at radio source “I” is embedded close to IRC2, obscured by  $\sim 60$  mag of visual extinction from dust grains both local to IRC2 and in intervening clouds along the line of sight. The combined heating contributions of the hot stars ionizing the compact H II regions “I” (near IRC2), “B” (the BN Object), and “L” (infrared source “n”), compact IRC objects (including 10 new peaks resolved here), and distributed near-infrared sources can account for the observed  $\sim 10^5 L_{\odot}$  total luminosity of the BN/KL complex.

*Subject headings:* infrared: ISM: continuum — ISM: individual (Orion-BN) —  
 ISM: individual (Orion Kleinmann-Low)

### 1. INTRODUCTION

It is not straightforward to determine the principal source of the  $\sim 10^5 L_{\odot}$  luminosity observed in the Orion Becklin-Neugebauer/Kleinmann-Low (BN/KL) complex, emerging in the infrared as thermal emission from heated, distributed dust grains. Early observations showed that IRC2 (a compact 12  $\mu\text{m}$  source with no significant near-infrared counterpart) had an exceptionally deep 9.7  $\mu\text{m}$  silicate absorption feature and appeared to be extended, which suggested that IRC2 was an unusual and very luminous object (Downes et al. 1981). The early observational results are discussed in §§ 3.3.1. and 5.2 and summarized in the comprehensive review by Genzel & Stutzki (1989, see pp. 62 and 76 for discussion of IRC2 images).

A single O star or several early B stars embedded within the complex could account for the observed infrared luminosity. However, at the time that the last detailed model was proposed (Wynn-Williams et al. 1984) there was no observational evidence for such luminous stars, which contributed to the widely accepted view that IRC2 was the principal luminosity source in the BN/KL complex. Two compact H II regions (radio continuum point sources) were subsequently detected in the heart of BN/KL at 15 and 22 GHz with the Very Large Array (VLA): “B” coincident with the BN Object and “I” coincident with the Orion SiO maser (Churchwell et al. 1987; Garay, Moran, & Reid 1987). Then Menten & Reid (1991, 1995) made the important discovery of a third H II region “L” at 22 GHz within the core of BN/KL.

Gezari (1992) used the VLA radio source positions with new 8.7  $\mu\text{m}$  image data to show that the peak of IRC2 was

displaced from SiO/I by  $0''.8 \pm 0''.2$  and suggested that an unseen luminous stellar object associated with radio source I powered the SiO maser (rather than the infrared emission from IRC2), in which case neither IRC2 nor the Orion SiO maser would be unique objects in the Galaxy. In the initial report of the work presented here (Gezari & Backman 1994) we concluded that (1) IRC2 is much less luminous than previously believed; (2) a luminous star, which could provide some external heating to IRC2, should be present at the I position next to the IRC2 dust cloud; (3) luminous stars associated with the three compact H II regions found within BN/KL may be the more significant luminosity sources (rather than IRC2) for the complex; and (4) IRC2 is a significant distance ( $\sim 5''$ ) from the center of expansion of the low-velocity maser outflow (Genzel et al. 1981), while the compact H II region L lies within the center-of-expansion error box. Menten & Reid (1995) independently reached the same conclusions, based on their 8 and 43 GHz VLA astrometry of the three compact radio continuum sources and the Orion SiO maser.

Mounting evidence for a variety of contributing luminosity sources prompts a reexamination of the accepted ideas about the BN/KL infrared complex and the nature of IRC2. We report here the results of a more detailed analysis of the infrared emission structure of BN/KL. The detailed color temperature and 9.7  $\mu\text{m}$  silicate dust extinction distributions are computed as images with  $\sim 1''$  resolution over the central field, using a complete set of nearly diffraction-limited array camera images at nine wavelengths between 4.8 and 20.0  $\mu\text{m}$ . We have used these results to derive more accurate physical properties and revised luminosities for IRC2 and the BN Object and to update the standard picture of Orion BN/KL.

### 2. INSTRUMENTATION AND OBSERVATIONS

#### 2.1. Array Camera System

The images presented here were made with a mid-infrared array camera system (Gezari et al. 1992) developed

<sup>1</sup> NASA/Goddard Space Flight Center, Code 685, Greenbelt, MD 20771.

<sup>2</sup> Visiting astronomer: NASA/Infrared Telescope Facility, which is operated by the Institute for Astronomy, University of Hawaii.

<sup>3</sup> Department of Physics and Astronomy, Franklin and Marshall College, P.O. Box 3003, Lancaster, PA 17604.

<sup>4</sup> Jet Propulsion Laboratory, California Institute of Technology, MS 247-767, 4800 Oak Grove Drive, Pasadena, CA 91109.

at NASA/Goddard using a  $58 \times 62$  pixel doped-silicon photoconductor array manufactured by Hughes/Santa Barbara Research Center (SBRC), a hybrid device based on the Hughes CRC-228 switched FET direct readout (DRO) multiplexer. The standard detector for  $4.8\text{--}12.4\text{ }\mu\text{m}$  observations is a gallium-doped silicon (Si:Ga) array. For the  $20.0\text{ }\mu\text{m}$  observations, an SBRC  $15\text{--}30\text{ }\mu\text{m}$  antimony-doped silicon (Si:Sb) array of the same design was provided by C. McCreight at NASA/Ames Research Center and installed in the array camera system. The Si:Ga and Si:Sb arrays are electronically interchangeable with only minor bias adjustments.

The optical design of the array camera (Gezari 1989) consists of a single off-axis length parabolic mirror, filter wheels, a cold aperture stop, and a system of baffles. The array detector, filters, and imaging optics were cooled to 10 K with liquid helium. This simple reflective optical design produces diffraction-limited  $5\text{--}14\text{ }\mu\text{m}$  images with negligible spatial distortion (less than  $1/2$  pixel across the array, or less than 1%). Out-of-field environmental background radiation rejection is better than 99%. The detector is a hybrid device based on a Hughes CRC-228 switched-FET direct readout (DRO) integrated circuit multiplexer. An OCLI Corporation  $4.4\text{--}14.5\text{ }\mu\text{m}$  circular variable filter (CVF) with transmission  $\sim 50\%$  and a filter wheel containing the broadband ( $\Delta\lambda/\lambda = 0.1$ ) OCLI "Silicate" interference filter set (listed in Table 1) are both mounted close to the cold stop. The spectral bandwidth of the CVF photometer is  $\Delta\lambda/\lambda = 0.04$  at  $10\text{ }\mu\text{m}$ , determined by the diameter of the adjacent cold stop. The array camera observing configuration at the Infrared Telescope Facility is summarized in Table 1.

The  $5\text{--}17\text{ }\mu\text{m}$  Si:Ga array was operated at about  $1/2$  full-well capacity (full well  $\sim 7 \times 10^5$  electrons using a  $\sim 30$  Hz frame rate; 30 ms integration time per pixel). The noise-equivalent flux density was NEFD =  $0.03\text{ Jy minute}^{-1/2}\text{ pixel}^{-1}$  ( $1\sigma$ ) at  $12.4\text{ }\mu\text{m}$  using the broadband ( $\Delta\lambda/\lambda = 0.1$ ) interference filter set. The NEFD expressed as noise-equivalent brightness is NEB =  $0.45\text{ Jy min}^{-1/2}\text{ arcsec}^{-2}$  ( $1\sigma$ ). For point sources, the NEFD  $\sim 0.5\text{ Jy min}^{-1/2}$  ( $1\sigma$ ) since the point source flux is spread over  $20\text{--}30$  pixels by diffraction and seeing. Observations were also made at  $18.1\text{ }\mu\text{m}$  with the Si:Ga array, operating at reduced quantum efficiency near the long wavelength cut-off of the detector. The antimony-doped silicon (Si:Sb) array was installed for the  $20.0\text{ }\mu\text{m}$  observations and operated in a similar manner

but was read out twice as fast (60 Hz) to compensate for the higher thermal background at  $20.0\text{ }\mu\text{m}$ .  $18.1$  and  $20.0\text{ }\mu\text{m}$  interference filters ( $\Delta\lambda/\lambda = 0.1$ ) were used. The Si:Sb detector was background limited, and the observational NEFD at  $20\text{ }\mu\text{m}$  was  $0.1\text{ Jy min}^{-1/2}\text{ pixel}^{-1}$  ( $1\sigma$ ). The noise-equivalent brightness at  $20.0\text{ }\mu\text{m}$  was NEB =  $1.5\text{ Jy min}^{-1/2}\text{ arcsec}^{-2}$  ( $1\sigma$ ). A complete description of the array camera system, including detector architecture, cryogenic optical instrument, electronics, and data acquisition system, is presented by Gezari et al. (1992).

## 2.2. Observations

The observations were made at the NASA Infrared Telescope Facility (IRTF) on Mauna Kea.  $12.4\text{ }\mu\text{m}$  images were obtained on the nights of 1988 March 15, 1988 November 11, and 1989 March 23;  $8.7$  and  $9.8\text{ }\mu\text{m}$  images were made on the night of 1988 November 11, and a complete set of  $7.8\text{--}12.4$  and  $18.1\text{ }\mu\text{m}$  images was made on the night of 1990 December 4. The  $20.0\text{ }\mu\text{m}$  mosaic image was obtained on the night of 1989 November 9, and the  $4.8\text{ }\mu\text{m}$  image was made on the night of 1991 March 21. The observed image profile measured from calibration stars under good atmospheric conditions was typically  $1''.1 \pm 0''.1$  FWHM at  $12.4\text{ }\mu\text{m}$ . The IRTF chopping secondary mirror was driven at 3 Hz with the reference beam  $40''$  to the north. Detailed discussions of sky subtraction, flat-fielding, and photometric calibration procedures are presented by Gezari et al. (1992), and Gezari (1995). Data reduction and image analysis were done with the MOSAIC software package (Varosi & Gezari 1993) written in the Interactive Data Language (IDL).

## 2.3. Photometric Calibration

Standard-star calibration fluxes have not previously been established at all of our filter wavelengths. Flux densities corresponding to 0.0 mag were extrapolated to our filter wavelengths from the mid-infrared absolute flux calibration established by Rieke, Lebofsky, & Low (1985), i.e.,  $0.0\text{ mag} = 36.0 \pm 1.2\text{ Jy}$  at  $10.6\text{ }\mu\text{m}$  and  $9.4 \pm 0.5\text{ Jy}$  at  $21.0\text{ }\mu\text{m}$ . Photometric calibration of the BN/KL images was made using  $\alpha$  Canis Majoris as the primary infrared standard. The photometric calibration values adopted here for  $\alpha$  CMA were extrapolated from a fit to photometric data for  $\alpha$  CMA between  $1.65$  and  $10\text{ }\mu\text{m}$  given in the list of Bright Infrared Standard Stars compiled at the NASA/Infrared Telescope

TABLE 1  
OBSERVING CONFIGURATION ON THE IRTF TELESCOPE

Parameter	Value
Pixel size (arcsec) .....	$0.260 (\pm 0.003)$
Array field of view ( $\alpha, \delta$ ) (arcsec).....	$15.0 \times 16.1$
Diffraction limit ( $1.22 \lambda/D$ ) (arcsec)	
$4.8\text{ }\mu\text{m}$ .....	0.36
$12.4\text{ }\mu\text{m}$ .....	0.93
$20.0\text{ }\mu\text{m}$ .....	1.60
Chopper frequency (Hz) .....	3
Chopper throw (arcsec) .....	40 (north)
Frame rate (Hz)	
at $5\text{--}17\text{ }\mu\text{m}$ .....	30
at $20\text{ }\mu\text{m}$ .....	60
Integration time (minutes) .....	1 (1800 frames at 30 ms each)
Fixed filters ( $\mu\text{m}$ ) <sup>a</sup> .....	7.8, 8.7, 9.8, 10.3, 11.6, 12.4, 18.1, 20.0
Circular variable filter ( $\mu\text{m}$ ) <sup>b</sup> .....	4.4–14.5

<sup>a</sup>  $\Delta\lambda/\lambda \sim 0.1$ , transmission  $\sim 0.8$ .

<sup>b</sup>  $\Delta\lambda/\lambda = 0.04$  at  $10\text{ }\mu\text{m}$ , transmission  $\sim 0.5$ .

Facility, and to observations at 18 and 20  $\mu\text{m}$  listed in the Catalog of Infrared Observations (Gezari et al. 1993). The magnitude of  $\alpha$  CMa increases monotonically from  $-1.38$  mag at 4.8  $\mu\text{m}$  to  $-1.46$  mag at 20  $\mu\text{m}$ , with an estimated uncertainty of  $\sim 0.02$  mag.

The internal uncertainty of flux measurements within a single image (relative photometry) is estimated to be  $\pm 2\%$  of the peak at BN, limited by the effectiveness of flat-fielding procedures. The absolute calibration uncertainty is estimated at  $\pm 10\%$ , primarily because of the variability of atmospheric transmission during the observations and interpolation of the calibration-star flux data to our wavelengths.

The observed relative 18.1  $\mu\text{m}$  brightness distribution is accurate for all sources except the BN Object, for which it may be inaccurate because of a possible small near-infrared light leak in the 18.1  $\mu\text{m}$  filter. All of the other IRc objects are very weak near-infrared sources, and any near-infrared light leak contribution is negligible compared to their 18.1  $\mu\text{m}$  fluxes. The 18.1  $\mu\text{m}$  flux-calibration standard was IRc4 (assumed peak brightness 55 Jy arcsec $^{-2}$  at 18.1  $\mu\text{m}$ ). The uncertainty in absolute 18.1  $\mu\text{m}$  flux is estimated to be  $\pm 30\%$ . Therefore the 18.1  $\mu\text{m}$  image data are useful primarily for relative photometry or structural analysis.

#### 2.4. Astrometric Calibration

Astrometric precision of array image data is limited by several factors, including optical distortion (pin-cushion, etc.), plate scale error (due to uncertain magnification, focus differences, lack of astrometric standards in the infrared, encoder accuracy), chopper stability, and field rotation (mechanical mounting of the array in the camera and the camera on the telescope).

The plate scale of the  $58 \times 62$  pixel array camera at the Cassegrain focus of the IRTF was measured to be  $0''.260 \pm 0''.003$  pixel $^{-1}$  in both right ascension and declination, with a corresponding field of view of  $15''.0 \times 16''.1$  ( $\alpha$ ,  $\delta$ ). The relative positions of stellar sources in a single image can be determined to an accuracy of better than 0.5 pixel, or  $\pm 0''.1$ , by centroid fitting of Gaussian image profiles. Considering these combined effects, relative source positions in a single array field can be determined with an experimental error of  $\pm 0''.012$  per arcsecond of angular distance measured, but not less than  $\pm 0''.1$ . Details of the astrometric calibration method are described in detail by Gezari (1992).

Calibration of absolute mid-infrared positions in BN/KL is difficult because there are no nearby stars with well-determined positions that are also strong mid-infrared sources. Gezari (1992) registered the mid-infrared and 22 GHz VLA position reference frames and determined that the best position for the infrared pointlike core of the BN Object was  $\alpha = 5^{\text{h}}32^{\text{m}}46^{\text{s}}.64 \pm 0''.01$ ,  $\delta = -5^{\circ}24'16''.5 \pm 0''.1$  (1950), the Menten & Reid (1991) VLA position for B, which we use here as the absolute infrared position reference for the BN/KL images.

### 3. RESULTS

#### 3.1. The Mosaic Images and the 4.8–20.0 $\mu\text{m}$ Data Set

Figure 1 shows the center of a 12.4  $\mu\text{m}$  mosaic covering a  $25'' \times 30''$  field of view, assembled from 12 overlapping images. Figure 2 gives the 12.4  $\mu\text{m}$  calibrated brightness contours. Figure 3 shows the large-scale 20.0  $\mu\text{m}$  mosaic image of BN/KL covering a  $40'' \times 40''$  field of view, assembled from 23 individual overlapping  $15''.0 \times 16''.1$

images. Figure 4 gives the calibrated brightness contours. Significant 20.0  $\mu\text{m}$  emission extends over most of the field, and real diffraction-limited ( $1''.6$ ) structure is apparent down to the 1 Jy arcsec $^{-2}$  brightness level. Figure 5 shows enlarged detail in the extended 20.0  $\mu\text{m}$  emission from the eastern region of BN/KL (see § 3.2). The positions of the compact IRc sources and the 2 cm continuum point sources described in § 1 are presented schematically in Figure 6.

Figures 7 and 8 present the calibrated image data set of the central  $\sim 17''$  field at our nine wavelengths between 4.8 and 20  $\mu\text{m}$ . Dramatic differences in the observed brightness distribution can be seen between the images in the clear continuum (7.8, 12.4, and 20.0  $\mu\text{m}$ ) and those showing the effects of silicate absorption (9.8, 10.3, and 18.1  $\mu\text{m}$ ), discussed further in § 3.3.2. This complete image data set is used for photometry of the compact sources and is the basis for the analysis that follows.

#### 3.2. New Mid-Infrared Sources in BN/KL

A total of 10 new mid-infrared peaks, listed in Table 2 and illustrated in Figures 5 and 6, have been identified in the images. Following the general nomenclature in BN/KL, we have assigned a new series of two-digit IRc numbers to eight of the new sources, IRc11–IRc17, and added position suffixes “NW” (northwest) and “N” (north) to two others, IRc4(NW) and IRc6(N). We have also adopted the names of the corresponding near-infrared sources (“n” and “IRc8”) for two other new mid-infrared objects. Although some of the new peaks appear relatively weak, high local silicate extinction may mask a more significant luminosity contribution they make to the region.

Two new compact sources IRc11 and IRc12, which are most prominent at 12.4  $\mu\text{m}$ , have been detected about  $4''$  and  $6''$  east of IRc2, respectively. Two additional new sources, IRc 13 and IRc 14, appear in the 20.0  $\mu\text{m}$  extended emission located about  $9''$  east of IRc2 (enlarged in Fig. 4). We have assigned the names IRc15–IRc17 to three significant clumps that are seen in the extended plateau emission about  $3''$  southeast, east, and northeast of BN in the 20.0  $\mu\text{m}$  image. These correspond to more diffuse, anonymous 2.1  $\mu\text{m}$  continuum emission features. IRc15 also corresponds to a strong knot of 2.12  $\mu\text{m}$  H $_2$  emission in the new NICMOS image of BN/KL (Stolovy et al. 1998), while IRc16 and IRc17 correspond to weaker H $_2$  sources. IRc18 is an extended source lying about  $7''$  south of IRc2. IRc8 nearby has not previously been detected at mid-infrared wavelengths.

An enigmatic new compact source, which we call IRc4(NW), is seen about  $2''$  northwest of IRc4. It seems to be an extension off the northwest end of the bright, extended IRc4 20  $\mu\text{m}$  source. However, this unusually compact object is seen distinctly only in the 8.7  $\mu\text{m}$  image (Fig. 4), where it is comparable in brightness to IRc2 and IRc7 and is considerably brighter than IRc4. IRc4(NW) is not prominent as a compact source at any other wavelength. A new, very compact source, which we call IRc6(N), is seen about  $1''$  north of source IRc6, appearing most prominently in the 7.8 and 8.7  $\mu\text{m}$  images. The 3.8  $\mu\text{m}$  point source n (Lonsdale et al. 1982; Gezari 1992) appears clearly about  $2''$  south and  $1''$  east of IRc7 in many of the images (Fig. 4), particularly at 8.7  $\mu\text{m}$ , where it is clearly defined against the extended emission. The enhanced 8.7  $\mu\text{m}$  emission exhibited by IRc4(NW), IRc6(N), and n could be due to the 8.6  $\mu\text{m}$  polycyclic aromatic hydrocarbon (PAH) dust

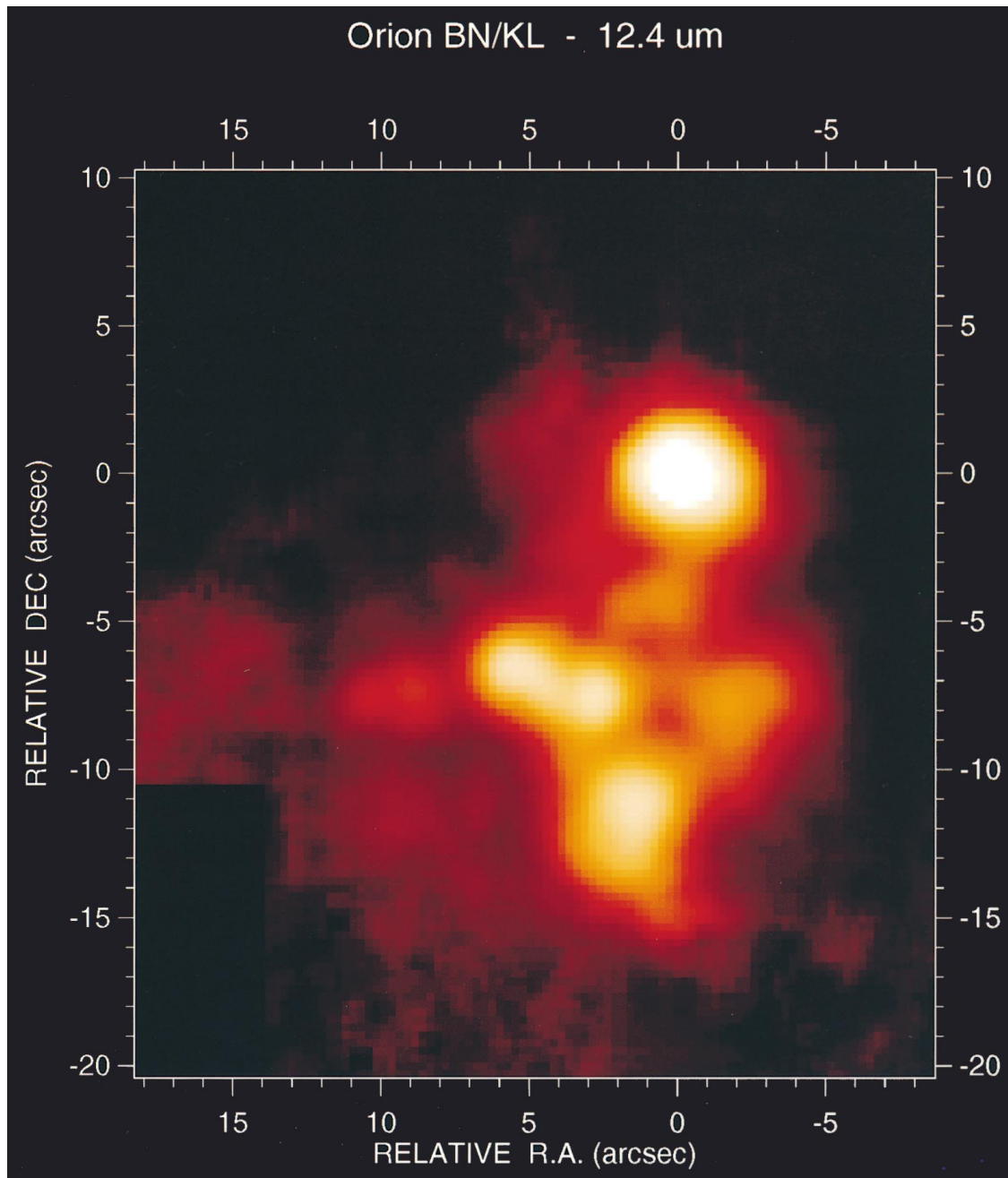


FIG. 1.—12.4  $\mu\text{m}$  mosaic array image of Orion BN/KL assembled from 12 overlapping 1 minute exposures obtained with the Si:Ga  $58 \times 62$  array camera, displayed with a logarithmic intensity scale to enhance faint structure. The compact IRC sources and their positions relative to the BN Object are listed in Table 2. The brightest 12.4  $\mu\text{m}$  source in the image is the BN Object at  $151 \text{ Jy arcsec}^{-2}$ . The  $1\sigma$  noise level is  $0.15 \text{ Jy arcsec}^{-2}$ . Position offsets are measured from the BN Object ( $\Delta\alpha, \Delta\delta = 0, 0$ ).

grain spectral feature, although comparable brightening that might be expected from the 7.8 and 11.3  $\mu\text{m}$  PAH lines, which are frequently observed (see Bientema et al. 1996; Molster et al. 1996), is not obvious in the corresponding 7.8 and 11.6  $\mu\text{m}$  filters.

### 3.3. Structure of IRC2 and IRC7

#### 3.3.1. Background

Early  $\sim 2''$  resolution aperture photometry observations of IRC2 (see, e.g., Rieke, Low, & Kleinmann 1973; Wynn-Williams & Becklin 1974; Grasdalen, Gherz, & Hackwell 1981; Lee et al. 1983) had shown it to be quite extended ( $3'' \times 5''$ ). Greatly improved knowledge of the IRC2 source profile and position was obtained from one-dimensional

speckle interferometry observations of IRC2 at 4.9  $\mu\text{m}$  (Chelli, Perrier, & Lena 1984) and linear scans through IRC2 at 7.8 and 12.5  $\mu\text{m}$  along  $45^\circ$  baselines (Lester et al. 1985), showing that IRC2 was very compact but not clearly resolving it from IRC7. The one-dimensional spatial measurements were by nature ambiguous, and the results could be interpreted variously as emission from a disk, a torus, or from an embedded compact object. Gezari (1992) made  $\sim 1''$  resolution 8.7 and 12.4  $\mu\text{m}$  imaging observations showing that IRC2 and IRC7 were independent, very compact sources. Plambeck, Wright, & Carlstrom (1990) presented SiO maser velocity field results as evidence for an expanding, rotating  $0''.15$  diameter disk structure (a size scale well below our imaging spatial resolution in the mid-

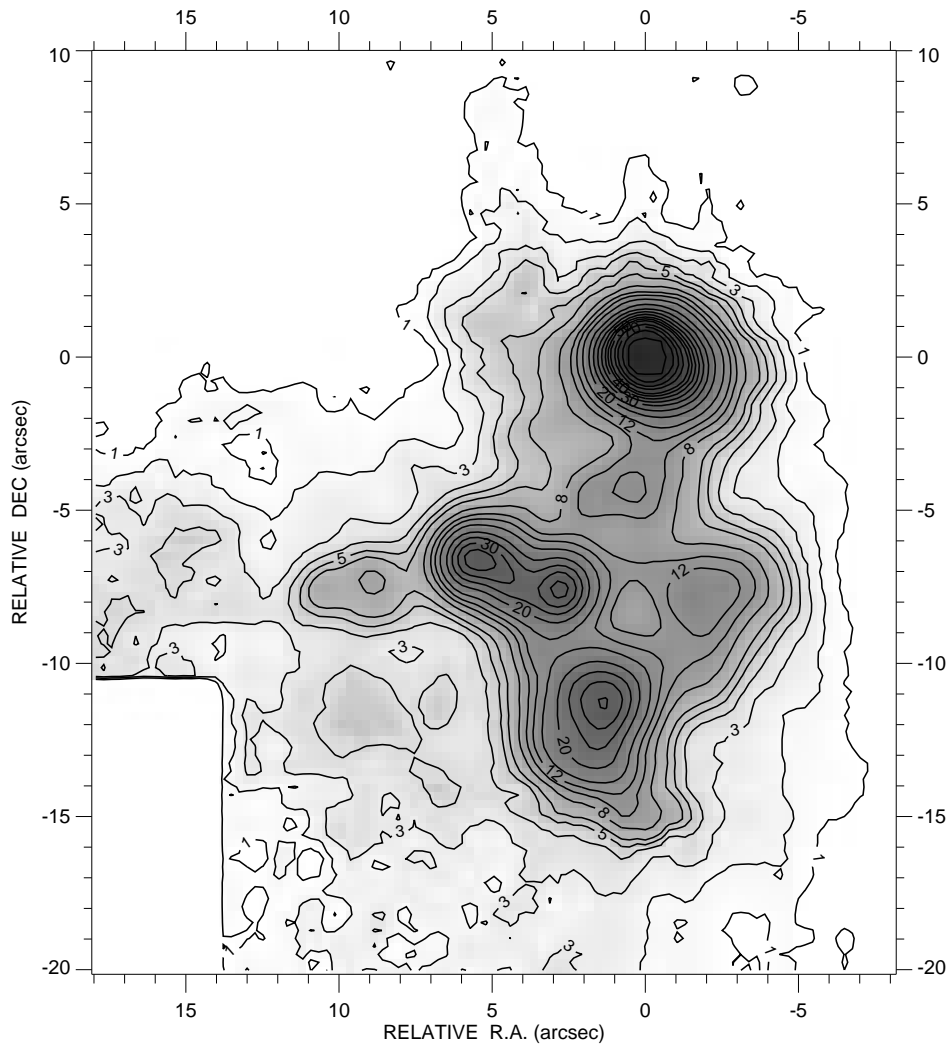


FIG. 2.—Brightness contours of the  $12.4\ \mu\text{m}$  mosaic array image of Orion BN/KL (Fig. 1). The brightest source in the image is the BN Object (0, 0) at  $151\ \text{Jy arcsec}^{-2}$ . The lowest contour is  $1\ \text{Jy arcsec}^{-2}$  and the  $1\sigma$  noise level is  $0.15\ \text{Jy arcsec}^{-2}$ .

infrared). Wright et al. (1990) recognized an apparent offset between the peak of IRC2 and the SiO maser, but at that time the size of the offset was comparable to the positional errors of the infrared astrometric observations.

### 3.3.2. New Results for IRC2 and IRC7

IRC2 and IRC7 are resolved at  $12.4\ \mu\text{m}$  (Figs. 1, 2, 7, and 8) as two equally bright point sources (Table 2). A narrow, partially resolved ridge of emission extends westward and slightly south from IRC2 directly toward IRC7. IRC2 and IRC7 are separated by  $2''.9 \pm 0''.1$  (a projected distance of about 1500 AU at 450 pc). The ridge that connects IRC2 and IRC7 appears to be curving slightly around the position of the 15 GHz source I in individual short-exposure  $12.4\ \mu\text{m}$  images (Gezari, Folz, & Woods 1989). The morphology suggests erosion of the ridge by luminous sources near the SiO maser position. While IRC2 is slightly elongated toward IRC7 and the source pair has a general dumbbell-like appearance, we do not see evidence in the mid-infrared array data to support the idea that these two sources together represent a torus of material seen nearly edge-on (previous speculation summarized by Genzel & Stutzki 1989; see pp. 62 and 76 for discussion of IRC2 images).

Several other sources and features are located  $\sim 1''$  southeast of IRC2, including the Orion SiO maser, the molecular hot core peak (Masson & Mundy 1988, and references therein), the  $450\ \mu\text{m}$  continuum emission peak (Wright et al. 1992), the 3 mm continuum peak (Murata et al. 1992; Wright, Plambeck, & Wilner 1996), and the deepest  $9.8\ \mu\text{m}$  silicate line absorption (see § 4.1). The observations of Dougados et al. (1993) show that IRC2 breaks up into a cluster of distinct sources at  $3.8\ \mu\text{m}$ , suggesting the presence of several embedded stars.

Images of IRC2 taken in the deepest part of the broad silicate absorption feature (using the  $9.8$  and  $10.3\ \mu\text{m}$  filters; Fig. 4) show that the details of the observed structure of IRC2 change dramatically at  $9.8\ \mu\text{m}$  as compared with the adjacent continuum. At  $9.8\ \mu\text{m}$  IRC2 is more extended southeastward toward the SiO maser position. There are also significant differences between the  $9.8$  and  $10.3\ \mu\text{m}$  images themselves, a puzzling effect that cannot be easily explained. At  $10.3\ \mu\text{m}$ , only the narrow ridge is visible and the southerly extension from the IRC2 peak position toward the SiO maser is absent. These structural differences are real and, despite the weakness of the source in the silicate images, not due to noise or array gain defects.



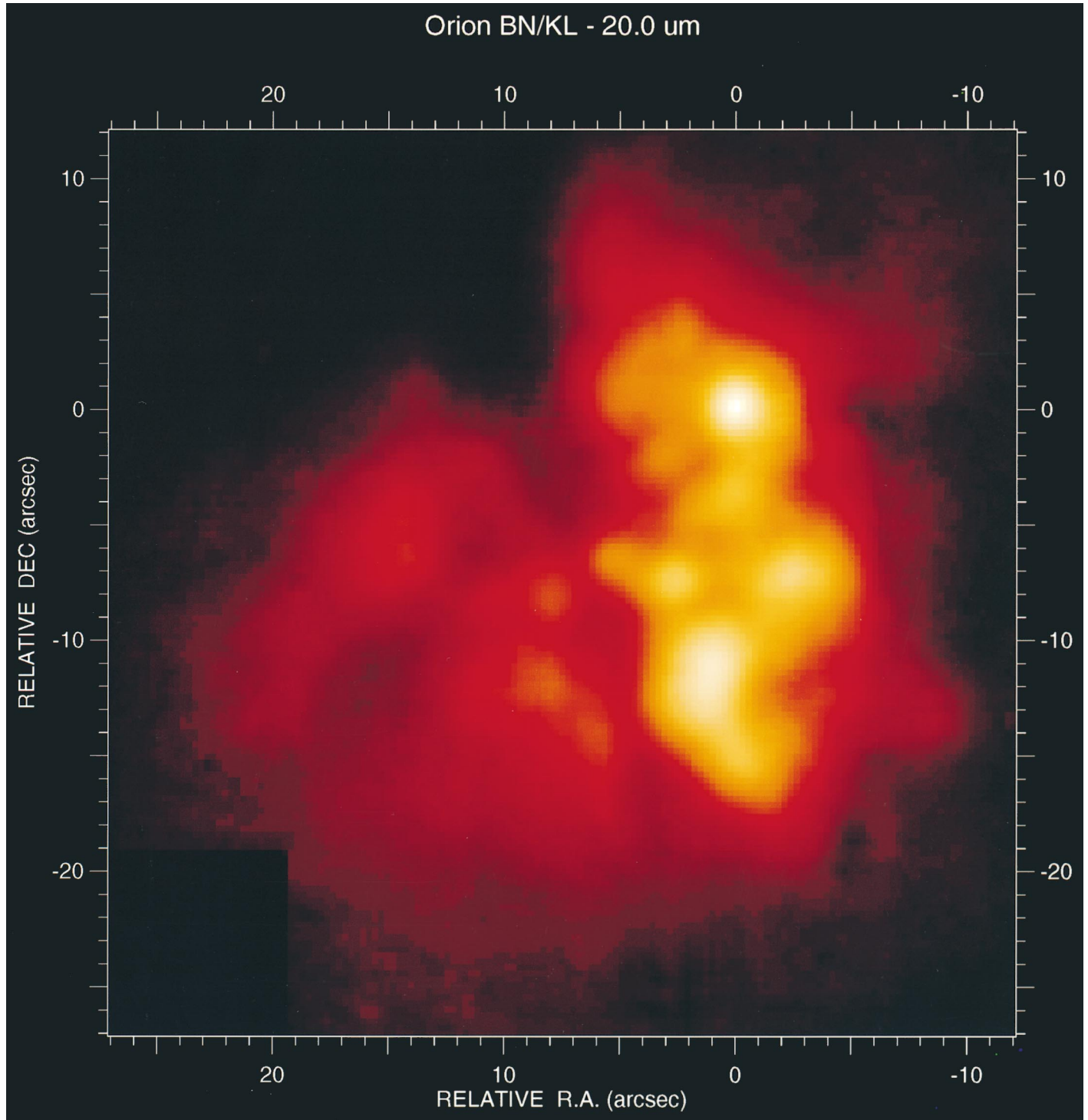


FIG. 3.—20.0  $\mu\text{m}$  mosaic array image of the Orion BN/KL complex obtained with an Si:Sb  $58 \times 62$  array installed in the camera. This figure shows diffraction-limited structure in a  $40'' \times 40''$  region, assembled from 23 individual  $15''.0 \times 16''.2$  images. The image is displayed with a logarithmic intensity scale from the noise level of  $1 \text{ Jy arcsec}^{-2}$  to the peak brightness of  $186 \text{ Jy arcsec}^{-2}$  at the BN Object. The bright, extended emission centered about  $10''$  south of BN (incorporating IRc 3, 4, and 5) comprises the KL Nebula. Position offsets are measured from BN (0, 0).

### 3.4. Photometry of Compact Sources

Simultaneous relative photometry at each wavelength can be obtained for all sources in the core of the BN/KL infrared cluster from the final coadded array image data set (Fig. 7). The infrared surface brightness of features in the images was sampled in a  $3 \times 3$  pixel ( $0''.8 \times 0''.8$ ) square synthetic aperture, relative to the peak brightness of BN at each wavelength. Table 2 presents the peak brightness (Jy

$\text{arcsec}^{-2}$ ) and the position at which the brightness was sampled in the “stack” of data images for 19 prominent compact infrared cluster sources in the central region of BN/KL.

Many of the IRc sources are observed against an extended background of emission, complicating the determination of the total flux densities of the individual compact sources. IRc4 becomes blended with extended

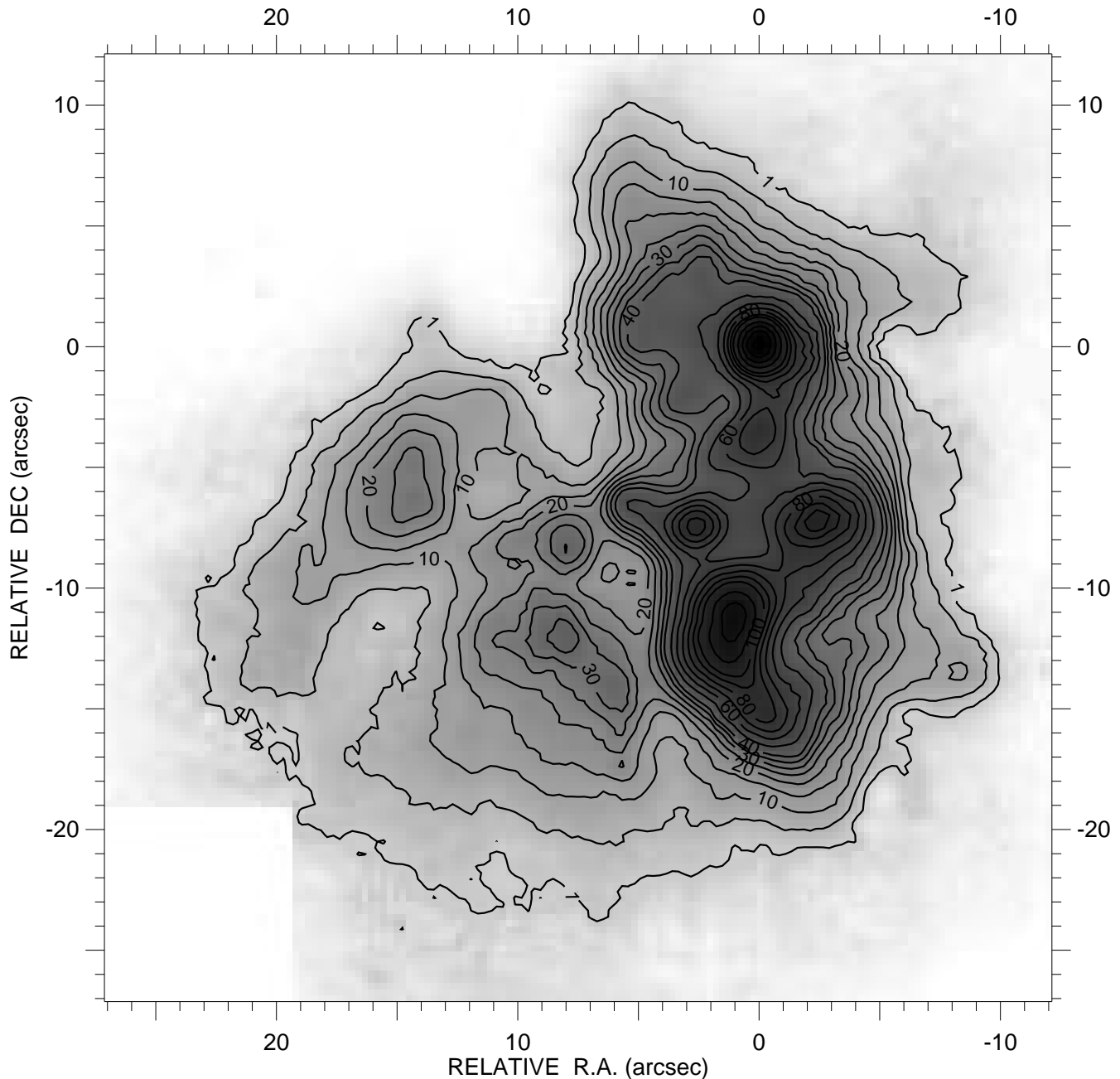


FIG. 4.—Brightness contours of the  $20.0\ \mu\text{m}$  mosaic array image of the Orion BN/KL complex (Fig. 3). The peak brightness is  $186\ \text{Jy arcsec}^{-2}$  at BN. The lowest contour level is  $1\ \text{Jy arcsec}^{-2}$ . Clumpy extended emission in the eastern half of the image and new sources in the plateau east of BN are slightly cooler material not readily detected at shorter wavelengths, suggesting that the region is more complex and contains more embedded luminous sources than previously believed.

emission at the longer wavelengths, and the BN Object (the relative photometric calibration reference; see Table 2) itself is surrounded by a significant extended plateau source component. Total flux densities can be calculated by integrating over the brightness distribution in the image data and subtracting any underlying plateau contribution. When individual source total flux densities were required in our analysis, the plateau contribution was subtracted by measuring the flux densities in  $9 \times 9$  and  $13 \times 13$  pixel synthetic apertures for compact sources (specifically IRc2 and IRc7), or in  $15 \times 15$  and  $21 \times 21$  pixel apertures for more extended sources (such as BN). The flux density in the “frame” area between the smaller and larger boxes was taken to characterize the local, underlying plateau contribu-

tion, which was then subtracted from the flux in the central box (of equal area) to determine the corrected compact source total flux density. However, because of the subjective nature of these corrections, we have not calculated total flux densities for all of the compact sources in Table 2, but leave that interpretation to the individual researcher.

### 3.5. Positions of Compact Source Peaks

The positions of the peaks of some IRc sources change slightly with wavelength (by as much as  $\sim 0''.5$ ) relative to the peak of the BN Object. These are real displacements, which could be caused by the spatial distribution of silicate extinction and source color or source temperature gradients when observed over the large wavelength range of  $4.8\text{--}20.0$

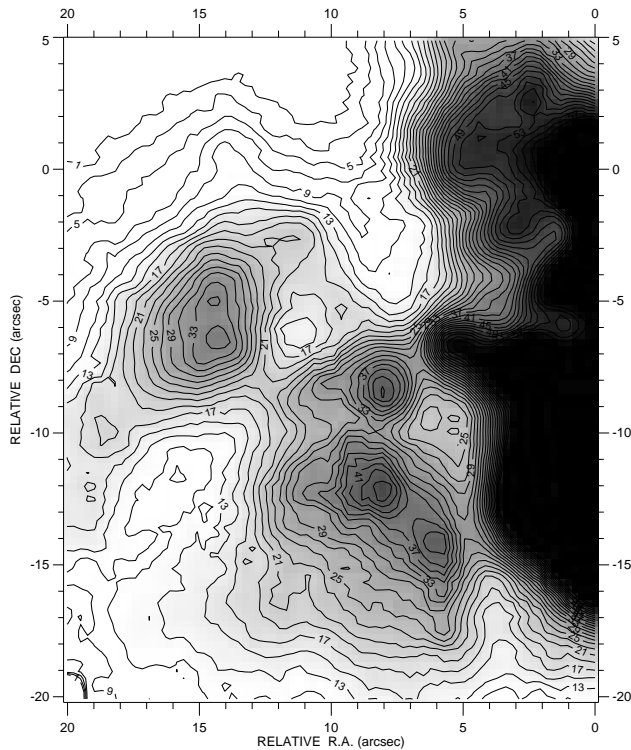


FIG. 5.—Eastern region of BN/KL at 20.0  $\mu\text{m}$  seen in Fig. 3, showing new emission detail including eight of the new compact mid-infrared source features (IRc11–IRc18) identified in Fig. 6. The contour interval is 2 Jy  $\text{arcsec}^{-2}$  plotted from the 1 Jy  $\text{arcsec}^{-2}$  level, and the brightest parts of the image are truncated to permit display of weaker features.

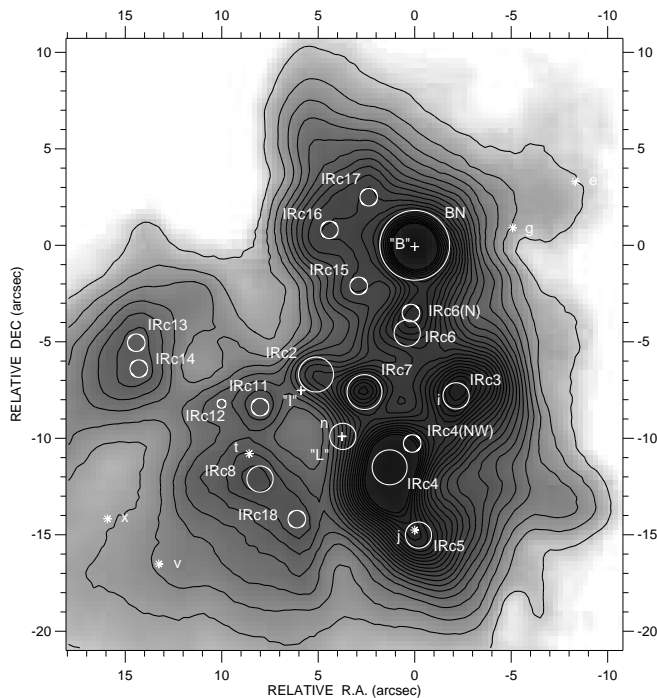


FIG. 6.—Schematic diagram showing the locations of the compact infrared (IRc) sources (circles) listed in Table 2. Compact H II regions (2 cm point sources; Menten & Reid 1991, 1995) indicated with crosses are I near IRc2, B, which coincides with the BN Object, and L, which coincides with infrared source n. Near-infrared sources (Lonsdale et al. 1982) are labeled with asterisks. The sizes of the symbols indicate relative mid-infrared brightness and are shown superimposed over the 20.0  $\mu\text{m}$  array image. The Orion SiO maser coincides with radio source I.

$\mu\text{m}$ . The measurement positions listed in Table 2 are nominal values but not necessarily the exact position of the source peak at every wavelength. IRc7 is the only compact source for which the peak position does not change by more than the errors ( $\pm 0''.1$ ) over our entire wavelength range or when going into and out of the broad 9.8  $\mu\text{m}$  silicate feature.

For example, IRc2 shifts peak position and is considerably rounder at 8.7  $\mu\text{m}$  compared to its structure at 12.4  $\mu\text{m}$  (see Fig. 8). At 8.7  $\mu\text{m}$  the peak of IRc2 is offset ( $\Delta\alpha, \Delta\delta = +5''.7, -6''.8$ ) from the peak of BN, while at 12.4  $\mu\text{m}$  IRc2 peaks at  $(+5.5, -6.6)$ . Radio source I and the SiO maser coincide and are offset  $(+5.9, -7.5)$  from BN, so the separation between IRc2 and I/SiO at 8.7  $\mu\text{m}$  is  $d = 0''.8 \pm 0''.1$  (in agreement with Gezari 1992), while at 12.4  $\mu\text{m}$  it is  $d = 1''.0 \pm 0''.1$ .

#### 4. DERIVED PHYSICAL PROPERTIES

##### 4.1. Silicate Absorption Line Strength

The strength of the 9.8  $\mu\text{m}$  silicate absorption feature, calculated over the whole field of view for each pixel in the mosaic, can be displayed as an image (Fig. 9). The 9.8  $\mu\text{m}$  absorption strength (calculated as the ratio of the 9.8  $\mu\text{m}$  peak brightness in a  $3 \times 3$  pixel aperture to the continuum interpolated between 7.8 and 12.4  $\mu\text{m}$ ) varies markedly among the IRc sources and is most dramatic in the vicinity of IRc2. The depth of the silicate absorption feature in IRc2 is a factor of 52 ( $A_{9.8} = 4.3$  mag) at 9.8  $\mu\text{m}$ , corresponding to  $A_v = 58$  mag visible extinction (uncertainty due primarily to the extinction law extrapolation). Using the same approach, the line-of-sight silicate absorption to the BN Object is only a factor of 3.0 (1.2 mag) at 9.8  $\mu\text{m}$ , corresponding to  $A_v = 17$  mag visible extinction.

Observations were also obtained in the 18  $\mu\text{m}$  silicate feature with the 18.1 filter. However, a lack of continuum data well outside the broad line, at 24  $\mu\text{m}$  for example, precluded further quantitative analysis. Brightness measured in the 20.0  $\mu\text{m}$  filter is also affected by absorption in the wings of the adjacent 18  $\mu\text{m}$  silicate absorption line; the effect is not as significant in the BN Object because of weaker silicate absorption strength there.

It seems likely that most of the absorbing grains toward heavily obscured IRc2–IRc7 cluster are close to those sources rather than distributed along the line of sight (discussed further in § 5.3) because the image of 9.8  $\mu\text{m}$  silicate strength (Fig. 9) shows structure that is generally associated with the mid-infrared sources, varying substantially from position to position in the field. In the region near IRc3 and IRc4, the absorption strength is uniform to within a factor of  $\sim 2$ , suggesting less extinction associated with source structure (considering the relatively smooth temperature distribution; see, e.g., Fig. 10) in this region.

##### 4.2. Extinction Corrections for IRc2 and BN

For the purposes of estimating the source color temperature and luminosity, the observations were dereddened using model extinction corrections based on the observed 4.3 mag strength of the 9.7  $\mu\text{m}$  silicate feature, extrapolated to longer and shorter wavelengths using the empirical interstellar extinction law of Rieke & Lebofsky (1985) and the dust grain optical constants of Draine & Lee (1984) for the region 12–20  $\mu\text{m}$ . We calculated the total flux densities for IRc2 and BN from the peak brightness data in Table 2 using the extended background subtraction procedure described in § 3.4. The observed brightnesses, the extinction corrections derived from them, the total flux densities, and



TABLE 2  
ORION BN/KL PHOTOMETRY

SOURCE	PEAK SOURCE BRIGHTNESS <sup>a</sup> (Jy arcsec <sup>-2</sup> )									MEASUREMENT POSITION <sup>b</sup> (arcsec)	
	4.8 $\mu$ m	7.8 $\mu$ m	8.7 $\mu$ m	9.8 $\mu$ m	10.3 $\mu$ m	11.6 $\mu$ m	12.4 $\mu$ m	18.1 $\mu$ m <sup>c</sup>	20.0 $\mu$ m	$\Delta\alpha$	$\Delta\delta$
BN Object .....	58	155	125	66	88	121	151	...	186	0.0	0.0
IRc2 .....	1.0	16.5	2.5	0.5	0.9	7.5	33	30	55	+5.7	-6.8
IRc3 .....	0.7	<0.5	<0.5	0.6	1.4	4.0	12	40	96	-1.6	-8.0
IRc4 .....	<0.5	1.9	0.7	1.0	2.5	11	30	55	143	+1.5	-11.4
IRc5 .....	0.9	0.6	<0.5	<0.5	0.9	2.8	8.4	...	93	-0.2	-14.7
IRc6 .....	1.2	1.0	0.8	0.6	1.1	3.8	11	30	79	+0.5	-4.3
IRc7 .....	0.4	4.9	1.8	0.8	1.8	9.2	32	40	98	+2.8	-7.7
IRc8 .....	<0.5	<0.5	<0.5	<0.5	0.4	0.7	3.6	...	45	+8.3	-12.0
n .....	1.2	2.7	1.3	0.8	(1.5)	(3.1)	(11)	(15)	(48)	+3.6	-9.9
New mid-infrared sources											
IRc4(NW) .....	<0.5	1.0	1.9	0.6	1.4	3.9	13	45	(106)	0.0	-10.5
IRc6(N) .....	1.7	1.4	1.9	1.0	1.3	3.8	9.6	35	85	-0.1	-3.6
IRc11 .....	<0.5	1.0	<0.5	0.5	0.5	1.4	6.0	...	32	+9.0	-7.4
IRc12 .....	<0.5	1.6	...	...	0.6	0.8	6.3	...	26	+10.3	-7.6
IRc13 .....	...	...	...	...	...	...	2.4	...	36	+14.4	-4.9
IRc14 .....	...	...	...	...	...	...	2.8	...	37	+14.3	-6.4
IRc15 .....	1.0	0.5	<0.5	0.5	0.7	1.8	6.0	(5)	53	+3.0	-2.1
IRc16 .....	0.7	<0.5	0.6	<0.5	<0.5	1.3	3.5	(10)	52	+4.6	+0.7
IRc17 .....	1.7	...	...	...	...	...	2.8	...	54	+2.4	+2.6
IRc18 .....	<0.5	<0.5	<0.5	<0.5	0.8	<0.5	2.1	5	42	+6.2	-14.0

<sup>a</sup> Peak source brightness (Jy arcsec<sup>-2</sup>; 1 Jy =  $10^{-26}$  W m<sup>-2</sup> Hz<sup>-1</sup>), uncorrected for and including any underlying extended emission at each source position, measured in a  $3 \times 3$  pixel ( $0''.78 \times 0''.78$ ) box relative to BN at all wavelengths. The absolute calibration uncertainty is  $\pm 10\%$ ; the uncertainty in relative brightness at each wavelength is  $\pm 2\%$ . Upper limits are in parenthesis, and occur when a compact source is not distinct from the surrounding extended emission. Total flux densities can be calculated from the brightness contours in each individual case (see § 3.4).

<sup>b</sup> Position at which the image brightness was measured. Some of the compact source peak positions shift slightly with wavelength because of extinction effects (see § 3.5). The relative position offset is from the BN Object ( $\alpha = 5^h32^m46^s.64 \pm 0^s.01$ ,  $\delta = -5^\circ24'16''.5 \pm 0''.1$ , epoch 1950). Error in determining peak positions is  $\pm 0''.1$  (about one-half pixel).

<sup>c</sup> Absolute 18.1  $\mu$ m brightness uncertainty is estimated to be  $\pm 30\%$  (figures in italics) because of limited 18.1  $\mu$ m flux calibration data. The observed brightness of BN is undetermined because of a possible near-infrared light leak; this effect is negligible for the other IRc sources, which were calibrated relative to IRc4.

TABLE 3  
DEREDDENED OBSERVATIONS OF IRC2 AND BN

$\lambda$ ( $\mu$ m)	OBSERVATIONS		EXTINCTION CORRECTION <sup>b</sup>		DEREDDENED TOTAL FLUX DENSITY <sup>c</sup> (Jy)
	Peak Brightness (Jy arcsec <sup>-2</sup> )	Total Flux Density <sup>a</sup> (Jy)	$A_{\lambda}$ (mag)	Factor	
IRc2					
4.8 .....	1.0	5	1.4	3.6	18
7.8 .....	16	55	0.9	2.3	125
9.8 .....	0.5	2	4.9	91	180
12.4 .....	33	120	1.6	4.4	530
20.0 .....	55	240	1.4	3.6	860
BN Object					
4.8 .....	58	260	0.4	1.4	360
7.8 .....	155	370	0.3	1.3	480
9.8 .....	66	160	1.4	3.6	580
12.4 .....	151	600	0.5	1.6	960
20.0 .....	186	1390	0.4	1.4	1950

<sup>a</sup> Total source flux density calculated by summing the observed brightness in a  $9 \times 9$  pixel ( $2''.3$ ) square aperture for IRc2, and in  $15 \times 15$  pixels ( $3''.9$ ) for the more extended BN Object. The background subtraction procedure used is described in § 3.4.

<sup>b</sup> Computed using the interstellar extinction law of Rieke & Lebovsky 1985 as well as the dust optical constants of Draine & Lee 1984, based for IRc2 on the observed 9.8  $\mu$ m silicate absorption factor of 52 ( $A_\lambda = 4.3$  mag) and for BN on an observed absorption factor of 2.3 ( $A_\lambda = 0.9$  mag).

<sup>c</sup> Extinction-corrected total source flux density, used in luminosity estimates.

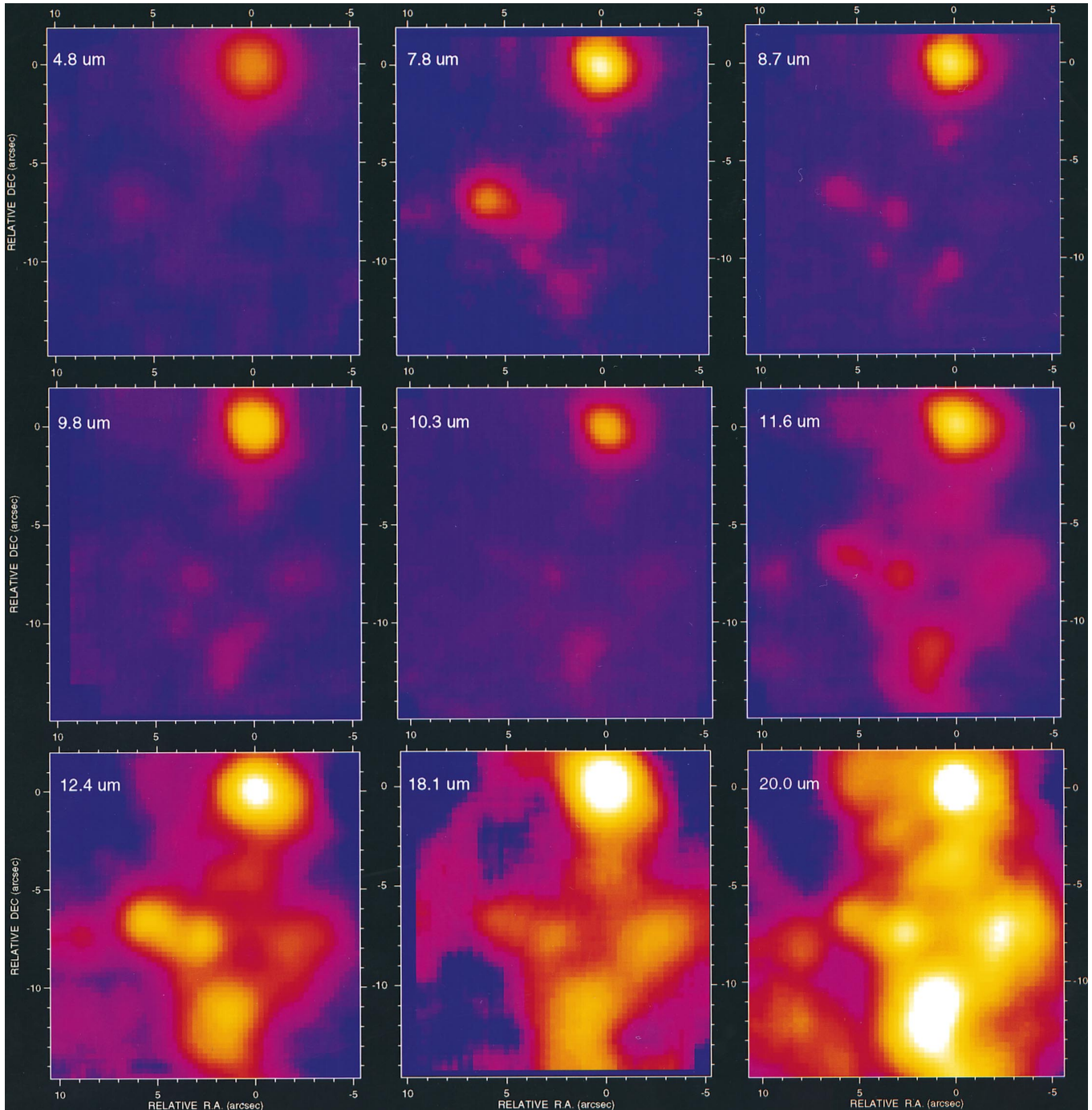


FIG. 7.—Images of the BN/KL core showing structure around the prominent IRC sources and the BN Object (0, 0) at 4.8  $\mu\text{m}$ , 7.8  $\mu\text{m}$ , and 8.7  $\mu\text{m}$  (top row); 9.8  $\mu\text{m}$ , 10.3  $\mu\text{m}$ , 11.6  $\mu\text{m}$  (middle row); and 12.4  $\mu\text{m}$ , 18.1  $\mu\text{m}$ , 20.0  $\mu\text{m}$  (bottom row). The nearly diffraction-limited images resolve the original  $3'' \times 5''$  “IRC2” source into a group of objects including the strong 12.4  $\mu\text{m}$  point sources IRC2 and IRC7 and several compact mid-infrared sources within a few arcseconds of IRC2. Dramatic structural differences are seen because of the effects of the broad silicate spectral absorption features at 9.7 and 18  $\mu\text{m}$ . The pixel size is  $0''.26$ . All of the images are displayed with the same logarithmic intensity scale. The approximate intensities in  $\text{Jy arcsec}^{-2}$  are 1–5 (faint red), 5–15 (red), 15–30 (orange), 30–100 (yellow), and  $>100$  (white) (see Fig. 8 and Table 2 for brightness values).

the dereddened total flux densities are given in Table 3 for IRC2 and BN.

Color temperatures were derived from the observed continuum brightness data, and luminosities were estimated from the extinction-corrected total flux density spectra.

### 4.3. Temperature Distribution

#### 4.3.1 Color Ratio “Image”

The first-order dust temperature distribution can be approximated from color ratios using various combinations

of the dereddened 3.8, 7.8, 12.4, and 20.0  $\mu\text{m}$  array data. Figure 10 shows an “image” of the 12  $\mu\text{m}$ /20  $\mu\text{m}$  color ratio with  $1''$  resolution over the central  $30'' \times 40''$  region of BN/KL, calculated from the observed 12.4 and 20.0  $\mu\text{m}$  mosaic images (Figs. 1 and 3). The regions of highest dust temperature should indicate the locations of the principal luminosity sources, based on the simple argument that temperature gradients trace the direction of energy flow, although local extinction effects must be considered in this interpretation.

The highest temperatures derived from the 12/20  $\mu\text{m}$

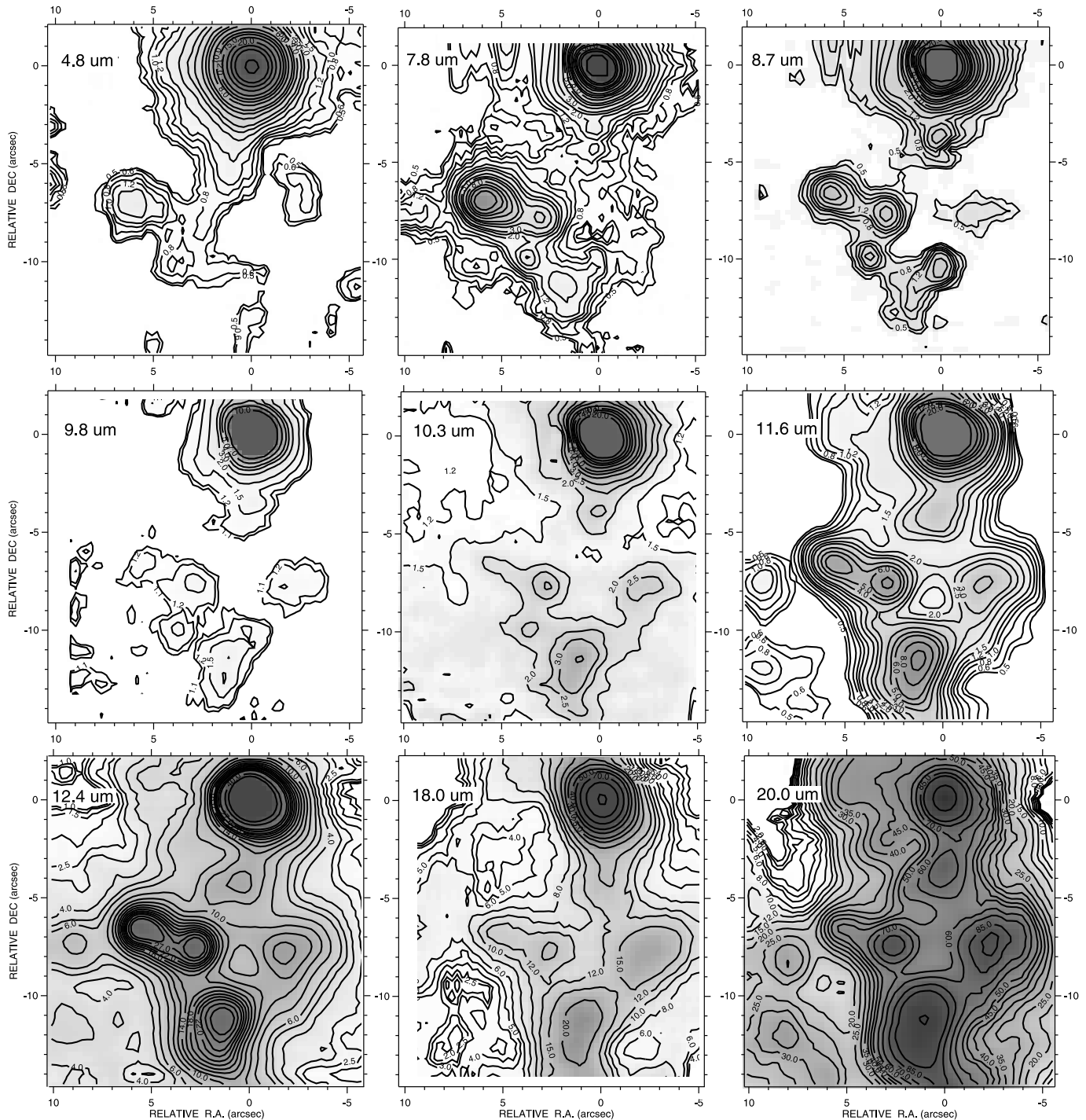


FIG. 8.—Contour maps of the Orion BN/KL core at 4.8, 7.8, and 8.7  $\mu\text{m}$  (top row), 9.8, 10.3, and 11.6  $\mu\text{m}$  (middle row), and 12.4, 18.1, and 20.0  $\mu\text{m}$  (bottom row), showing structure around the BN Object (at 0, 0) and the prominent IRC sources. The data were generally binned to  $3 \times 3$  pixels (the weaker 4.8, 9.8, and 18.1  $\mu\text{m}$  images were binned to  $5 \times 5$  for comparable signal-to-noise ratios). The pixel size is  $0''.26$  and the images are fully sampled (diffraction limit  $\lambda/D = 0''.4$  at 5  $\mu\text{m}$ ,  $0''.8$  at 10  $\mu\text{m}$ , and  $1''.6$  at 20  $\mu\text{m}$ ). The contour interval is quasi-logarithmic, in  $\text{Jy arcsec}^{-2}$  as labeled. The sources can be identified using Fig. 6.

image ratio occur at BN and in an extended area that includes IRC2/IRC7, IRC4, and, notably, the two new compact sources IRC11 and IRC12, located  $\sim 5''$  east of IRC2. This region roughly coincides with the molecular “hot core” (Mangum, Wooten, & Plambeck 1993; Wright et al. 1996) and the 450/800  $\mu\text{m}$  emission peak (Wright et al. 1992). It is noteworthy that, with our high spatial resolution, the warm dust is still confined to the vicinity of BN and IRC2, suggesting that luminosity sources in BN/KL are located in those parts in the complex.

#### 4.3.2. Color Temperature Calculation

The entire dereddened 4.8–20.0  $\mu\text{m}$  spectrum cannot easily be fit by a single-temperature blackbody source spectrum. Line-of-sight temperature gradients in the sources result in a flattening of the observed spectrum over a large wavelength range, especially in the case of BN, which is a strong near-infrared source compared to others in the complex. To estimate realistic temperatures characteristic of specific source components, color ratios over interme-

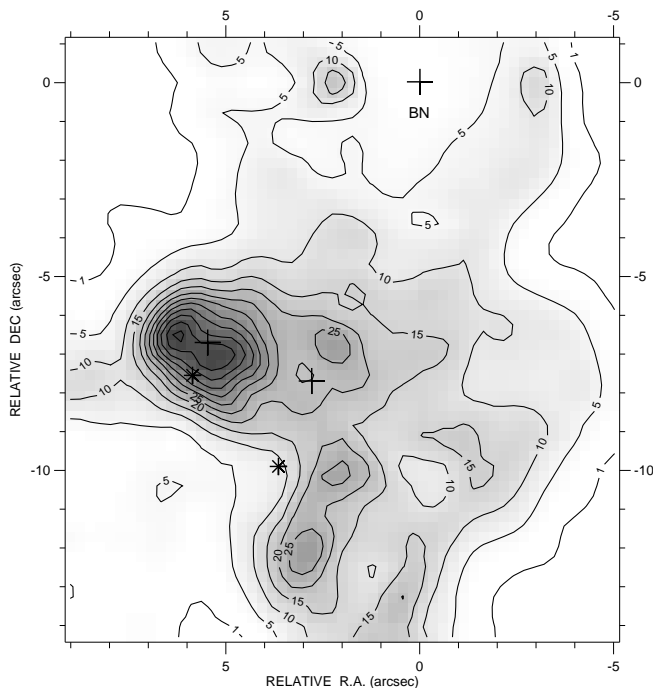


FIG. 9.—Silicate extinction factor, the  $9.8\ \mu\text{m}$  line-to-continuum ratio. The peak  $9.8\ \mu\text{m}$  absorption occurs near IRc2 (a factor of 52). Strong absorption is generally correlated with mid-infrared source structure where it occurs, suggesting that the extinguishing grains are local to the individual sources. The contour interval is 5 units. Crosses mark the positions of the BN Object (0, 0), IRc2 (5, -7) and IRc7 (3, -8), and asterisks mark radio sources I (6, -8) and L (4, -10).

diate spectral intervals ( $7.8\text{--}12.4\ \mu\text{m}$ , or  $12.4\text{--}20.0\ \mu\text{m}$ , for example) were considered more reliable. Color temperatures were calculated from the dereddened observed brightness for two cases: dust emissivity  $\epsilon(\lambda)$  constant with wavelength (simple blackbody) and a dust emissivity law  $\epsilon(\lambda) \propto \lambda^{-1}$ .

Because of the complexity of the silicate spectrum, color temperatures were calculated using combinations of continuum wavelengths of  $4.8$ ,  $7.8$ ,  $12.4$ , and  $20.0\ \mu\text{m}$ , avoiding contamination by the silicate spectral absorption features at  $9.7$  and  $18\ \mu\text{m}$ . In the case of IRc2, the broad  $18\ \mu\text{m}$  silicate absorption feature may significantly depress the  $20.0\ \mu\text{m}$  observed brightness, resulting in somewhat elevated color temperatures calculated with simple blackbody models from ratios including the  $20.0\ \mu\text{m}$  data, as discussed in § 4.3.2.

#### 4.3.3. Color Temperatures for IRc2 and BN

The dereddened  $7.8$ ,  $12.4$ , and  $20.0\ \mu\text{m}$  flux densities yield color temperatures for IRc2 of about 240 K for model grain emissivity cases  $\epsilon(\lambda) = \text{constant}$ , and about 200 K for  $\epsilon(\lambda) \propto \lambda^{-1}$  [an  $\epsilon(\lambda) \propto \lambda^{-1}$  dependence results in lower physical grain temperatures]. These temperatures ( $\sim 200$  K) are significantly cooler than the findings of Wynn-Williams et al. (1984), who concluded that IRc2 had the dereddened spectrum of a  $700 \pm 200$  K blackbody.

The color temperature of the BN Object (calculated from the corrected  $12\ \mu\text{m}/20\ \mu\text{m}$  ratio assuming simple blackbody spectra) is  $T_c = 460$  K, in agreement with previous determinations (see, e.g., Wynn-Williams et al. 1984). The emission ratio between  $12$  and  $20\ \mu\text{m}$  characterizes the warm, extended dust component; the pointlike core of BN is much hotter. Interpretation of the photometry is complicated by the strength of BN over a large spectral range

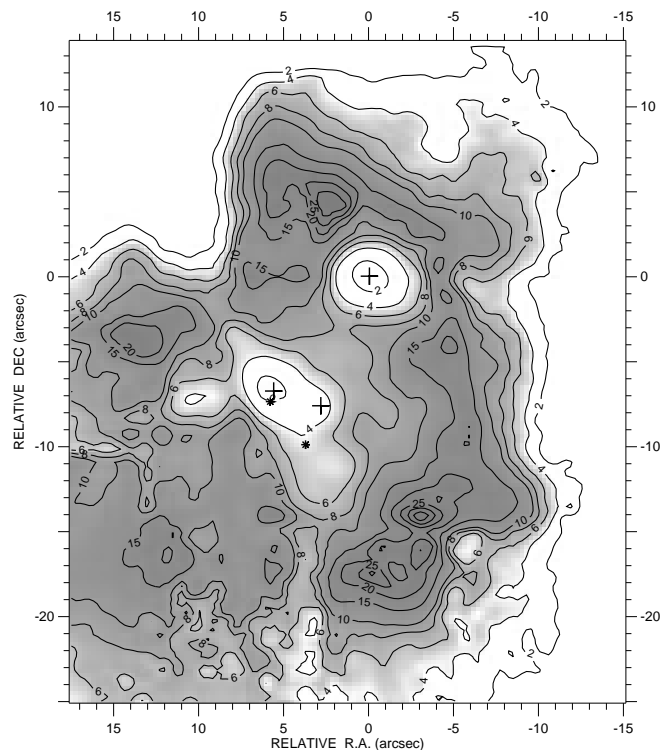


FIG. 10.—Directly observed  $20.0\ \mu\text{m}/12.4\ \mu\text{m}$  brightness ratio in BN/KL, analogous to the color temperature distribution (lighter regions are hotter). The lowest observed ratio (highest temperature) occurs at BN, corresponding to a dereddened color temperature of  $T_c = 460$  K [assuming  $\epsilon(\lambda) = \text{const.}$ ]. Nearly comparable ratio values are found in an extended region containing IRc2, IRc7, IRc11, IRc12, and the molecular “hot core,” about  $10''$  southwest of BN. For IRc2, color temperatures are  $T_c = 240$  K taking  $\epsilon(\lambda) = \text{const.}$  and  $T_c = 200$  K with  $\epsilon(\lambda) \propto \lambda^{-1}$ . Crosses mark the positions of BN (0, 0), IRc2 (5, -7) and IRc7 (3, -8), and asterisks mark radio sources I (6, -8) and L (4, -10).

(indicative of large radial temperature gradients), as well as its extended structure and the consequent problem of effectively correcting for the plateau contribution (§ 3.4).

### 4.4. New Luminosities for IRc2, BN, and BN/KL

#### 4.4.1 Luminosity Calculation

We recalculated the luminosity of IRc2 by fitting a simple blackbody model spectrum to the extinction-corrected total flux density spectra (see Table 3), assuming that the radiation from IRc2 is isotropic and that the silicate feature is not filled in by emission from foreground sources. A more elaborate model (which incorporates varying ratios of silicate and graphite grains in the emitting source and along the line of sight) produced similar luminosity results. However, a preferred Si/C abundance ratio could not be identified because the limited spectral range of the observations did not adequately constrain the fit. Because extinctions derived from dereddened spectra are slightly higher than extinctions calculated from uncorrected data, the new luminosity estimates for BN and IRc2 represent upper limits.

#### 4.4.2. IRc2

We find that the apparent infrared luminosity of IRc2 is only  $L = 1000 \pm 500 L_\odot$ , dramatically lower than previous values, which are as high as  $\sim 10^5 L_\odot$  (summarized in the review by Genzel & Stutski 1989). This luminosity is calculated from a fit to the dereddened total flux density data (Table 3). The corresponding optically thick source is

$T = 300$  K and  $\Omega = 1.1 \times 10^{-12}$  sr (diameter  $\sim 0''.05$ ) with visual extinction  $A_v = 58$  and no significant warm emitting dust surrounding it. A more realistic optically thin cloud of 300 K dust grains extending over a  $\sim 1$  arcsec<sup>2</sup> area would have an opacity  $\tau(12 \mu\text{m}) \sim 0.01$  and would be opaque to the short-wavelength radiation from an embedded stellar source. While the results can be taken only as first order estimates, it is clear that the luminosity of IRC2 need be only  $L \sim 1000 L_\odot$  to account for the observed mid-infrared image data.

The 30  $\mu\text{m}$  maps by Wynn-Williams et al. (1984) suggest that substantial luminosity is emerging at wavelengths  $\lambda > 20 \mu\text{m}$ . However, the presence of a cool dust emission component at  $\lambda > 30 \mu\text{m}$  raises our upper limit for the total luminosity of IRC2 to only  $L < 5000 L_\odot$ . Our diffraction-limited spatial resolution shows that several sources (including BN, IRC3, IRC4, and IRC7) become brighter than IRC2 at  $\lambda > 20 \mu\text{m}$ . Therefore IRC2 cannot contribute more than a small fraction of the total 30  $\mu\text{m}$  luminosity (consistent with our 1000  $L_\odot$  estimate and 5000  $L_\odot$  upper limit). Our low luminosity result can be reconciled with the previous higher estimates, as discussed in § 5.1.

#### 4.4.3. BN Object

Using the same approach discussed above, the luminosity of the bright core of the BN Object is found to be about  $L = 2500 L_\odot$  (comparable to previous determinations) assuming a distance of 450 pc, with corresponding model parameters of  $T = 550$  K,  $A_v = 17$  mag, with the source becoming optically thick at a diameter of about  $0''.01$  ( $2.4 \times 10^{-13}$  sr). The luminosity and the model parameters for BN are consistent with emission from a substantial circumstellar dust cloud surrounding a main sequence B3–B4 star. Extended emission becomes from a much larger surrounding cool dust component prominent at  $\lambda > 20 \mu\text{m}$ . We estimate that the total luminosity from the extended ( $\sim 10''$  diameter) BN plateau region is  $L \sim 10^4 L_\odot$ .

#### 4.4.4. The Greater BN/KL Complex

The total bolometric luminosity of the entire Orion BN/KL source complex (central  $50''$ ) can be accurately estimated using our dereddened mid-infrared array data, far-infrared photometry (Beichman, Dyck, & Simon 1978; Thronson et al. 1978), the improved high spatial resolution submillimeter maps of Wright et al. (1992), and the 1 mm data of Elias et al. (1978). The overall peak of the spectrum appears to be near 50  $\mu\text{m}$ , so most of the luminosity would emerge in the wavelength decade shortward of that (i.e., in the 5–20  $\mu\text{m}$  band that we imaged). We assume that essentially all of the luminosity produced by sources in BN/KL is emitted or reradiated from within the central region considered here. From the mid-infrared, far-infrared, and submillimeter observations the total estimated flux in a  $50''$  aperture is  $\sim 1.3 \times 10^{-8} \text{ W m}^{-2}$ , corresponding to a total bolometric luminosity for BN/KL of  $L = 8 \times 10^4 L_\odot$  (assuming a distance of 450 pc and a nonfavored observer's position), consistent with previous determinations.

### 5. DISCUSSION

#### 5.1. Background

The idea that IRC2 was a very energetic object despite its modest mid-infrared brightness was supported by observations that showed that IRC2 coincided within the errors at that time with the Orion SiO Maser (Genzel et al. 1979) and was near the center of a systematic molecular gas

outflow traced by H<sub>2</sub>O and SiO maser emission (Genzel et al. 1981; Downes et al. 1982). The polarization data (Werner, Dinerstein, & Capps 1982) suggested that there were discrete clumps of scattering material as well as regions of localized low obscuration through which heated background material that accounted for much of the observed structure in BN/KL was viewed. IRC2 was also near the center of the 3.8  $\mu\text{m}$  polarization vector field. The only clearly self-luminous objects identified by these early investigations were the BN Object and IRC2. These results and the photometry and astrometry observations (summarized in § 3.3.1) all suggested that IRC2 was the dominant luminosity source in BN/KL, as set forth in the detailed model by Wynn-Williams et al. (1984).

In Gezari & Backman (1994) we noted that IRC2 was  $\sim 5''$  from the center of expansion of the low-velocity maser outflow (Genzel et al. 1981), while the compact H II region L lies within the  $\pm 0''.1$  by  $\pm 2''$  error box. Menten & Reid (1995) used 8 and 43 GHz astrometry to determine the precise location of the SiO maser relative to the H<sub>2</sub>O maser cluster and radio continuum point sources near IRC2 and concluded that other sources contribute significantly to the energetics of the Orion BN/KL region, particularly infrared source n, which coincides with their peculiar double radio source, and which they identified as being located within the  $1 \sigma$  error box of the H<sub>2</sub>O maser outflow.

#### 5.2. Reconciling the New IRC2 Luminosity with Previous Results

The luminosity we have calculated for IRC2 ( $L \sim 1000 L_\odot$ ) from the dereddened array data is 2–3 orders of magnitude lower than previous estimates (Downes et al. 1981; Wynn-Williams et al. 1984). Our results can be reconciled with those of Wynn-Williams et al. (1984) by considering several observational differences. The high luminosity estimates for IRC2 were based on early low-resolution aperture photometry showing a strong, extended ( $3'' \times 5''$ ) mid-infrared source. Because IRC2 and IRC7 were not resolved as separate objects, the measured flux of IRC2 was actually the sum of the two, which was further increased by the large extinction correction that was applied. Wynn-Williams et al. (1984) estimated the 3.8  $\mu\text{m}$  extinction toward IRC2 to be 8–11 mag, based on the assumptions that the highly polarized (40%) 3.8  $\mu\text{m}$  emission from IRC3 was scattered light and that IRC2 (the illuminating source) radiated isotropically. The high extinction estimate lead to a large color correction and consequently an excessively high derived color temperature ( $T = 700 \pm 200$  K) for IRC2. The results were consistent with a “hot,” luminous IRC2 and led to a corresponding correction of the IRC2 luminosity from an observed value of 500  $L_\odot$  up to  $0.5\text{--}2 \times 10^5 L_\odot$  (Wynn-Williams et al. 1984).

Our images resolve IRC2 and IRC7 as separate, compact sources, more accurately characterizing IRC2 independent of IRC7 and resulting in a lower observed flux density for IRC2. While the extinction to IRC2 calculated by Wynn-Williams et al. (1984) corresponds to  $\sim 4$  mag at 12  $\mu\text{m}$ , our high spatial resolution images in the 9.7  $\mu\text{m}$  silicate feature yield extinction to IRC2 of only  $\sim 1.9$  mag at 12.4  $\mu\text{m}$  where the spectrum of IRC2 peaks (almost an order of magnitude less attenuation than they adopted), further reducing the upward luminosity correction. Therefore both the dereddened flux density and the corrected color temperature we calculate for IRC2 are considerably lower than previous values.



Finally, even with a much lower luminosity IRC2 source than previously estimated, IRC2 could still be the source of the  $3.8\ \mu\text{m}$  emission scattered by IRC3. If IRC2 were a dense dust disk or torus oriented roughly edge-on to us so that the warm core of the disk is exposed in the general direction of IRC3, the hot inner regions could directly illuminate IRC3 but be obscured from us by the plane of the disk, and the IRC2 color temperature we observe would be that of the cooler outer regions of the disk. The warm core would have to have a temperature of only about 1000 K and a luminosity as low as  $5 \times 10^3 L_\odot$  to account for all of the observed  $3.8\ \mu\text{m}$  brightness of IRC3 as scattering of light from IRC2.

### 5.3. Dust Cloud Structure Near IRC2 and I

It is clear from the preceding discussion that extinction both from patchy line-of-sight clouds and circumstellar dust may complicate our view of the luminosity sources in BN/KL. Submillimeter and microwave observations (see, e.g., Wright et al. 1992; Mangum et al. 1993; Blake et al. 1996; Wright et al. 1996) have identified very dense clouds of dust and gas in the region. The observed anticorrelation of molecular emission and infrared sources demonstrates the role that extinction by cool dust in the foreground molecular clouds plays in the observed morphology of the infrared continuum emission.

The  $3.5\ \text{mm}$  continuum image by Wright et al. (1996) shows a cool,  $2'' \times 3''$  dust condensation centered about  $0''.5$  east of radio source I. This dense cloud could easily obscure a hot star such as the ionizing star for radio I. For example, only  $A_v = 20$  would be required to make an  $m_v = 1$  mag star at I undetectable at visible wavelengths. In the mid-infrared, the star could be detected only if it was surrounded by a dense circumstellar dust shell. However, no infrared counterpart has been detected, even at wavelengths as long as  $20\ \mu\text{m}$ , but given the small scale of the H II region and the fact that the SiO masers are located within  $\sim 0''.1$  of the radio continuum peak, one might expect that this source should be embedded in a cocoon of warm dust. For a luminosity  $L \sim 10^5 L_\odot$  and a size of  $\sim 0''.1$  (45 AU at the distance of the Orion Nebula), this warm dust cocoon would have a temperature of  $T \sim 1000\ \text{K}$ . At  $20.0\ \mu\text{m}$ , the longest wavelength we have used and the wavelength that probes most deeply, the flux from such a cocoon would be  $\sim 4000\ \text{Jy}$  in the absence of foreground extinction. However, the present mid-infrared array data sets a limit of  $\sim 60\ \text{Jy}$  for the observed  $20.0\ \mu\text{m}$  flux from the position of source I. Therefore,  $\sim 5\ \text{mag}$  of line-of-sight extinction would be required at  $20.0\ \mu\text{m}$  to reduce the flux from the cocoon around source I to this level. This is consistent with the observations of Wright et al. (1996) showing source I at the half-power contour of a dense clump of dust that has an average optical depth of  $\tau \sim 0.05$  at  $3.5\ \text{mm}$ , and that thus could have  $\tau > 5$  at  $20\ \mu\text{m}$ . IRC2 itself is further from the center of this dust condensation than I is and would suffer considerably less extinction, although perhaps enough to account for its strong silicate feature.

### 5.4. The New Picture

The arguments we have presented here suggest a scenario in which IRC2 is not the dominant luminosity source for the BN/KL complex. We have seen that it is clearly possible that several sources contribute substantially to the total luminosity of the BN/KL region. The color temperature peak (Fig. 10) and the orientation of the  $3.8\ \mu\text{m}$  polarization

vectors strongly suggest that the likely candidates for such luminosity sources are the putative hot stars that ionize the H II region I, and the stars associated with radio L and infrared n. We have resolved infrared source n from the extended background emission at 4.8, 7.8, 8.7, 9.8 and  $10.3\ \mu\text{m}$  (Fig. 4 and Table 2) and find that, compared to BN and IRC2, it is neither relatively bright nor has an unusually deep silicate absorption feature. Thus there is no indication from the present infrared data that n is an exceptionally luminous source in the infrared. However, the presence of the coincident compact H II region L clearly indicates the presence of an ionizing source (Menten & Reid 1995).

The ionizing star for compact H II region I would have to be B3 V type or earlier (Churchwell et al. 1987) corresponding to a luminosity of at least  $3 \times 10^3 L_\odot$ . Such a luminous star could be present within BN/KL but obscured by intervening dust, since the derived visible extinction to IRC2 is  $A_v = 58\ \text{mag}$  (see § 4.1). The suggestion of erosion of the mid-infrared contours on the south side of the IRC2–IRC7 ridge near I, seen most clearly in several of the best individual  $12.4\ \mu\text{m}$  images before coadding, is consistent with the idea that an early-type star is embedded at this position (see Fig. 14 in Gezari et al. 1989 for individual exposures; Fig. 2 in Gezari 1992 for the locations of I, the SiO maser, and the  $\text{H}_2\text{O}$  maser cluster near IRC2).

The hot star at radio source I could also contribute to the highly polarized scattered light observed from IRC3 and IRC4 since its radiation, illuminating IRC3/4, would be emitted perpendicular to the line of sight and need not be subjected to the extinction along the line of sight to IRC2 discussed above. In this scenario, even IRC2 could be illuminated and heated externally by the star at I. The  $3.8\ \mu\text{m}$  radiation from IRC2 should then be highly polarized, with electric vector oriented perpendicular to the line of sight to source I. Because of beam dilution, the orientation of the  $3.8\ \mu\text{m}$  electric vectors observed by Werner et al. (1983) was not well-enough determined to distinguish IRC2 from other illuminating sources. The higher angular resolution polarimetry observations by Minchin et al. (1991), Dougados et al. (1993), and Aitken et al. (1997) do show some suggestion of the changes in polarization angle with position expected if source I were, in fact, the dominant underlying  $3.8\ \mu\text{m}$  source. However, much higher ( $\sim 0''.1$ ) spatial resolution near-infrared polarimetry would be needed to clarify the respective roles of IRC2 and source I.

The distributions of silicate absorption line strength (Fig. 9) and color temperature (Fig. 10) show a local silicate absorption peak at IRC2 and local temperature peaks near IRC2 and BN, but otherwise there is little other small-scale extinction or temperature structure seen within the central  $\sim 20''$ . This supports the idea that IRC3 and IRC4 do not contain significant imbedded luminosity sources. Asymmetrically distributed circumstellar material and irregular foreground extinction are found to have a strong influence on the observed mid-infrared emission distribution. The hot star at I could be obscured by as much as  $\sim 60\ \text{mag}$  of visual extinction by dust grains in the IRC2 cloud and intervening material along the line of sight. The local extinction due to the dust cloud identified by Wright et al. (1996) is great enough to conceal a luminous object from view at  $\lambda < 20\ \mu\text{m}$ . Also, the fact that the line of sight to IRC2 passes through part of this cloud can account for its extremely deep silicate absorption feature.

What appears to be an extraordinary explosive event in Orion, imaged in  $1.64\ \mu\text{m}$  [Fe II] and  $2.12\ \mu\text{m}$   $\text{H}_2$  line



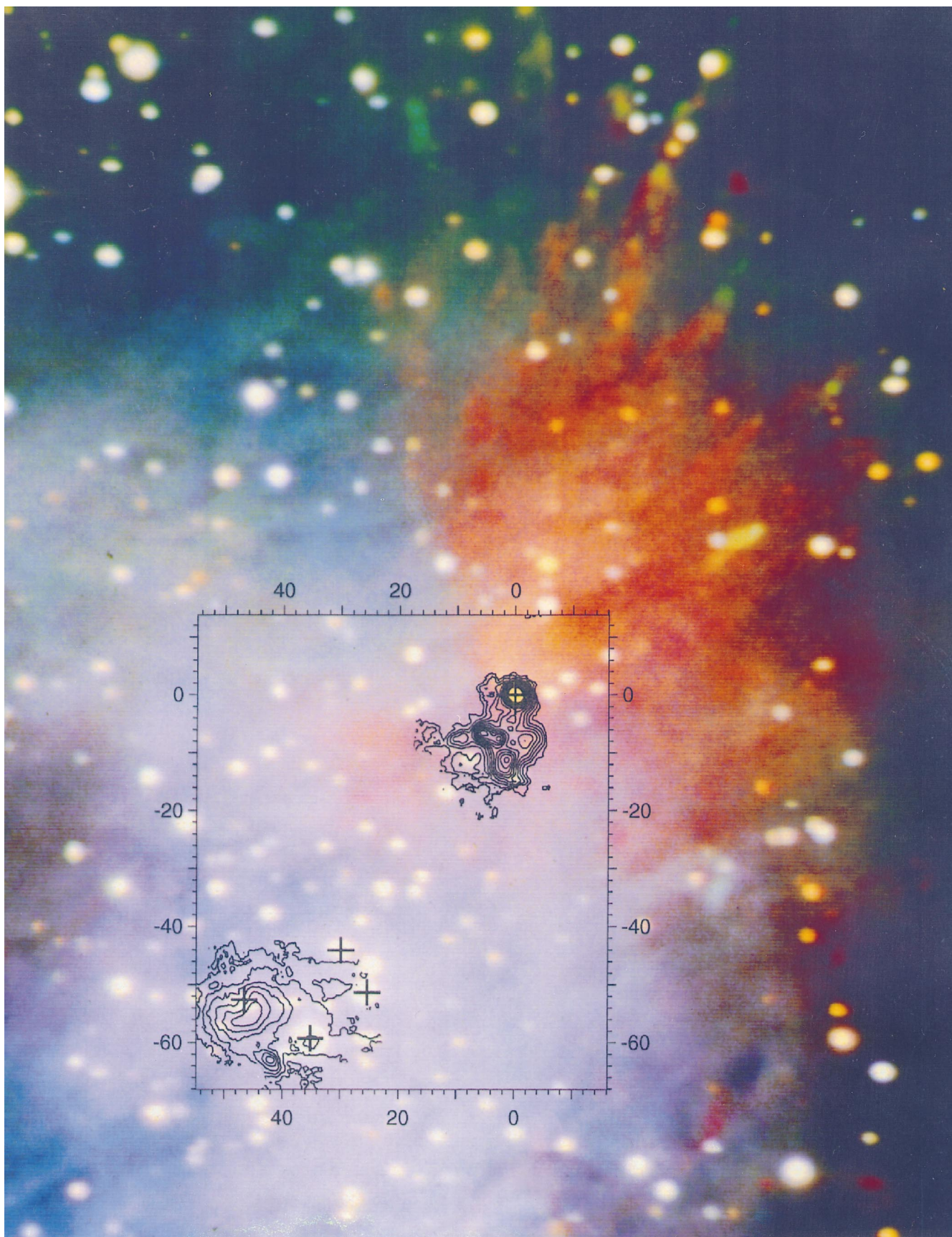


FIG. 11.—12.4  $\mu\text{m}$  continuum contours of BN/KL and the Ney-Allen Nebula superimposed over a portion of the three-color composite near-infrared image by Allen & Burton (1993) in the 1.25  $\mu\text{m}$   $J$ -band continuum (*blue*), the 1.64  $\mu\text{m}$  [Fe II] line (*green*), and the 2.12  $\mu\text{m}$   $\text{H}_2$  line emission (*red*). The red streamers (*upper right*) are purported to be the remnants of an extraordinary explosive event, which this comparison suggests originated in the northern regions of BN/KL close to BN (0, 0). The bright near-infrared source IRC9 (yellow point source located 23" north of BN) is another possible event origin site. The four Trapezium stars (*lower left* in contour map) are marked with crosses, and the extended 12.4  $\mu\text{m}$  emission near the star  $\theta^1\text{D Ori}$  (46, -52) is the Ney-Allen Nebula.

emission by Allen & Burton (1993), has variously been interpreted as a bipolar protostellar outflow, the interaction of stationary knots with an outflow, or a supernova event. Kundt & Yar (1997) proposed that the streamers are shock-illuminated remnants of stellar material from a supernova that occurred only  $\sim 10^2$  yr ago, which could have easily been obscured by dense dust clouds. Overlaying our 12.4  $\mu\text{m}$  wide-field mosaic of BN/KL and the Ney Allen Nebula on the composite  $[\text{Fe II}]\text{-H}_2$  image (Fig. 11) suggests that the origin of this energetic event (traced by jetlike streamers) is several arcseconds north and east of the BN Object. Stolovy et al. (1998) used NICMOS  $\text{H}_2$ -line images to conclude that the event origin was near IRC2, although the narrow  $\text{H}_2$  streamers are not distinct in the NICMOS images. Unfortunately, the diffuse structure of the  $[\text{Fe II}]$  and  $\text{H}_2$  streamers themselves (Fig. 11) simply does not allow for a precise determination of their origin; IRC2, the BN object, or several bright near-infrared stars near BN are all equally viable candidates. In any case, the possibility that another significant energetic process is occurring within BN/KL further argues against the simple view that a single source such as IRC2 dominates the region.

## 6. CONCLUSION

The results presented here are generally consistent with the Wynn-Williams et al. (1984) model for BN/KL regarding the basic structure of the infrared complex. However, the critical difference in the new picture that emerges is that IRC2 is not an object of high intrinsic luminosity and does not dominate the energetics of BN/KL. Although it is subject to high extinction, none of our results suggest that IRC2 itself is an unusual infrared source. We estimate that the infrared luminosity of IRC2 is only  $L \sim 1000 L_\odot$  (much lower than the generally accepted value). We conclude that IRC2 is a dense dust cloud of only moderate luminosity, heated internally by the embedded 3.8  $\mu\text{m}$  sources imaged

by Dougados et al. (1993) and externally by the nearby luminous star at compact H II region I.

This detailed study reinforces our previous conclusions (Gezari & Backman 1994) that the ionizing star for radio source I is a much more significant luminosity source in BN/KL than IRC2. The three radio point sources I, B, and L indicate the presence of luminous, ionizing sources in the core of BN/KL. It is likely that n is the origin of the low-velocity molecular outflow. Rather than attribute so much influence to IRC2, the combined contributions of luminous stars at the positions of the three compact H II regions, near-infrared stars associated with the well known IRC sources, and the new compact mid-infrared objects imaged in the complex together can account for the infrared luminosity of BN/KL.

We thank Frank Varosi for his continuing valuable contributions to the array camera program at NASA/Goddard and Craig McCreight and Mark McKelvey at NASA/Ames for their efforts toward the success of the 20  $\mu\text{m}$  observations. Walter Folz of NASA/Goddard and Mary Hewitt of Hughes/Santa Barbara Research Center played key roles in the successful development of the infrared array camera instrument. We thank Mark Reid and Karl Menten for useful discussions and for providing results prior to publication. We are grateful to Mike Hauser and Chuck Bennett for their support of the Array Camera Program at NASA/Goddard. Suvi Gezari contributed to the data analysis effort. Parts of this research were carried out at the Jet Propulsion Laboratory, California Institute of Technology, under contract to the National Aeronautics and Space Administration. The poi used to bless the array camera at the summit of Mauna Kea was provided by Jimmy's Drive-Inn of Hilo, Hawaii. This work was supported by NASA/OSSA RTOP 188-44-23-08.

## REFERENCES

- Aitken, D. A., Smith, C. H., Moore, T. J. T., Roche, P. F., Fujiyoshi, T., & Wright, C. M. 1997, *MNRAS*, 286, 85
- Allen, D. A., & Burton, M. G. 1993, *Nature*, 363, 54
- Beichman, C. A., Dyck, H. M., & Simon, T. 1978, *A&A*, 62, 261
- Beintema, D. A., et al. 1996, *A&A*, 315, L372
- Blake, G. A., Mundy, L. G., Carlstrom, J. E., Padin, S., Scott, S. L., Scoville, N. Z., & Woody, D. P. 1996, *ApJ*, 472, L49
- Chelli, A., Perrier, C., & Lena, P. 1984, *ApJ*, 280, 163
- Churchwell, E., Felli, M., Woods, D. O. S., & Massi, M. 1987, *ApJ*, 321, 516
- Dougados, C., Lena, P., Ridgway, S. T., Christou, J. C., & Probst, R. G. 1993, *ApJ*, 406, 112
- Downes, D., Genzel, R., Becklin, E. E., & Wynn-Williams, C. G. 1981, *ApJ*, 244, 869
- Downes, D., Genzel, R., Hjalmarsen, A., Nyman, L. A., & Ronnang, B. 1982, *ApJ*, 252, L29
- Draine, B. T., & Lee, H. M. 1984, *ApJ*, 285, 89
- Elias, J. H., et al. 1978, *ApJ*, 220, 25
- Garay, G., Moran, J. M., & Reid, M. J. 1987, *ApJ*, 314, 535
- Genzel, R., Moran, J. M., Lane, A. P., Predmore, C. R., Ho, P. T. P., Hansen, S. S., & Reid, M. J. 1979, *ApJ*, 231, L73
- Genzel, R., Reid, M. J., Moran, J. M., & Downes, D. 1981, *ApJ*, 244, 844
- Genzel, R., & Stutzki, J. 1989, *ARA&A*, 27, 41
- Gezari, D. Y. 1989, preprint
- . 1992, *ApJ*, 396, L43
- . 1995, *Proc. IAU Symp.* 167, *New Directions in Array Technology and Applications*, ed. A. G. Davis Phillip, K. A. Janes, & A. R. Upgren (Dordrecht: Kluwer), 97
- Gezari, D., & Backman, D. 1994, *Infrared Astronomy with Arrays: The Next Generation*, ed. I. McLean, *ASSL Vol. 190* (Dordrecht: Kluwer), 195
- Gezari, D. Y., Folz, W., & Woods, L. 1989, *Proc. Third Infrared Detector Technology Workshop*, NASA TM-102209 (Washington, DC: NASA), 267
- Gezari, D. Y., Folz, W., Woods, L., & Varosi, F. 1992, *PASP*, 104, 191
- Gezari, D. Y., Schmitz, M., Pitts, P., & Mead, J. M. 1993, *Catalog of Infrared Observations*, NASA RP 1294, (3d ed.; Washington, DC: NASA)
- Grasdalen, G. L., Gherz, R. D., & Hackwell, J. A. 1981, in *Proc. IAU Symp.* 96: *Infrared Astronomy* ed. C. G. Wynn-Williams & D. P. Cruikshank (Dordrecht: Reidel), 179
- Kundt, W., & Yar, A. 1997, *Ap&SS*, 254, 1
- Lee, T. J., Beattie, D. H., Geballe, T. R., & Pickup, D. A. 1983, *A&A*, 127, 417
- Lester, D. F., Becklin, E. E., Genzel, R., & Wynn-Williams, C. G. 1985, *AJ*, 90, 2331
- Lonsdale, C. J., Becklin, E. E., Lee, T. J., & Stewart, J. M. 1982, *AJ*, 87, 1819
- Mangum, J. G., Wooten, A., & Plambeck, R. L. 1993, *ApJ*, 409, 282
- Masson, C. R., & Mundy, L. G. 1988, *ApJ*, 324, 538
- Menten, K. M., & Reid, M. J. 1991, *BAAS*, 22(4), 1269 (abstract)
- . 1995, *ApJ*, 445, 157
- Minchin, N. R., et al. 1991, *MNRAS*, 248, 715
- Molster, F. J., et al. 1996, *A&A*, 315, L373
- Murata, Y., Kawabe, R., Ishiguro, M., Morita, K.-I., Hasegawa, T., & Hayashi, M. 1992, *PASJ*, 44, 381
- Plambeck, R. L., Wright, M. C. H., & Carlstrom, J. E. 1990, *ApJ*, 348, L65
- Rieke, G. H., & Lebofsky, M. J. 1985, *ApJ*, 288, 618
- Rieke, G. H., Lebofsky, M. J., & Low, F. J. 1985, *AJ*, 90, 900
- Rieke, G. H., Low, F. J., & Kleinmann, D. 1973, *ApJ*, 186, L7
- Stolovy, S., et al. 1998, *ApJ*, 492, L151
- Thronson, H. A., Harper, D. A., Keene, J., Lowenstein, R. F., Moseley, S. H., & Telesco, C. M. 1978, *AJ*, 83, 492
- Varosi, F., & Gezari, D. Y. 1993, in *ASP Conf. Proc.* 52, *Astronomical Data Analysis Software & Systems II*, ed. R. J. Hanisch, R. J. V. Brissenden, & J. Barnes (San Francisco: ASP), 393
- Werner, M. W., Dinerstein, H. L., & Capps, R. W. 1983, *ApJ*, 265, L13
- Wright, M., Sandell, G., Wilner, D. J., & Plambeck, R. 1992, *ApJ*, 393, 225
- Wright, M. C. H., Plambeck, R. L., & Wilner, D. J. 1996, *ApJ*, 469, 216
- Wright, M. C. H., Carlstrom, J. E., Plambeck, R. L., & Welch, W. J. 1990, *AJ*, 99, 1299
- Wynn-Williams, C. G., & Becklin, E. E. 1974, *PASP*, 86, 5
- Wynn-Williams, C. G., Genzel, R., Becklin, E. E., & Downes, D. 1984, *ApJ*, 281, 172